VeCell: A Fiji Plugin to unveil differences in spatio-temporal dynamics of macroglial cell development and proximity to blood vessels

Naomie Guille[1], Héloïse Monnet[1], Tristan Hourcade[1], Philippe Mailly[1], Martine Cohen-Salmon[1] and Anne-Cécile Boulay[1]

CIRB, Collège de France, Université PSL, CNRS, INSERM, 75005 Paris, France.

Corresponding author: anne-cecile.boulay@inserm.fr

Key-words: Sox9, Sox10, macroglial cell, cortical development, cell density, cell distribution, blood vessel, astrocyte, oligodendrocyte, OPC.

Funding statement

This work was funded by grants from Université PSL (Junior Fellow to ACB), ANR (VaMas to ACB) and the *Fondation pour la Recherche Médicale* (EQU202303016292 to MCS).

Abstract

Cortical development results from the proliferation, differentiation, migration and maturation of many cell types. While neuronal development has been extensively studied, the mechanisms regulating the development and maturation of macroglial cells (oligodendrocytes and astrocytes) are still largely to be determined. Here we present VeCell, a Fiji plugin designed to analyse the development of macroglial cells. Using immunolabeling for two transcription factors, Sox9 (specific to macroglial progenitors and astrocytes) and Sox10 (specific to oligodendrocyte lineage), we determined their density, distribution within and across cortical layers and distance to the blood vessels from postnatal day (P) 5 and P60 in the somatosensory cortex. We found that Sox9+ cells are evenly distributed in the cortex with regular intercellular distances and comparable densities between the upper and lower parts of the cortex. In contrast, Sox10+ cells are predominantly concentrated in the lower cortical layers, and exhibited a more random distribution with variable distances between cells. Finally, while confirming the increased density and branching of the vascular network after P5, we also showed that macroglial cells are closer to blood vessels from P15 onward. In summary, *VeCell* provides a valuable tool for analyzing the development and spatial organization of macroglial cells. Our findings in the cortex reveal distinct patterns of distribution and proximity to the vasculature for macroglial cells during postnatal development. These insights contribute to a deeper understanding of glial maturation and highlight the dynamic interplay between macroglial cells and the vascular network, offering new avenues for future research into brain development and function.

Introduction

The mammalian cortex is a complex and highly organized structure containing diverse neuronal, glial and vascular cell types. Cortical development is driven by highly regulated and coordinated sequences of cell proliferation, differentiation and migration, and requires the fine tuning of production/elimination and attraction/repulsion mechanisms. Neurons and macroglial cells - astrocytes and oligodendrocytes - are generated from common multipotent neural precursor cells (NPCs) (Miller and Gauthier, 2007). After neuron production, which starts around embryonic day (E) 12 and peaks at E15, NPCs switch to gliogenesis around E18 to sequentially generate astrocyte progenitors and oligodendrocyte precursor cells (OPC). Cortical astrocytes are produced mainly during the first postnatal week from a combination of delaminating NPCs and local proliferation of astrocyte progenitors following colonization of the cortical parenchyma (Clavreul et al., 2019; Ge et al., 2012). From the second postnatal week, their migration is halted and astrocytes mature both molecularly and morphologically to finally tile the brain with non-overlapping domains (Bushong et al., 2004, 2002; Halassa et al., 2007). Oligodendrocyte lineage cells (OligoLC) comprise both oligodendrocyte precursors (OPCs) and myelinating oligodendrocytes (Foerster et al., 2024). During cortical development, OPCs are produced in three spatiotemporal waves. In the postnatal cortex, OPCs generated in the first embryonic wave undergo massive cell death and are largely eliminated from the cerebral cortex by P10, progressively replaced by locally-produced OPCs from cortical progenitors (Kessaris et al., 2006). After birth, OPCs will progressively differentiate into oligodendrocytes (OLs) that form the myelin sheath around axons, mostly before the end of the 3rd postnatal week (Orduz et al., 2019). Some OPCs will remain in the adult brain, expressing the NG2 marker.

Cortical vascular network formation is initiated earlier than macroglial cells. Around embryonic day (E)9, the primary vascular network starts to form. From a perineural plexus, vascular sprouts invade the neuroectoderm by vasculogenesis and angiogenesis (Engelhardt, 2003). Postnatally, high angiogenesis rate results in an extensive vascular expansion between P8 and P12. New blood vessels (BVs) arising from ascending veins give rise to a dense capillary bed (Coelho-Santos and Shih, 2020).

BVs and macroglial cells interact during postnatal development. OPCs from ventral origin use blood vessels to migrate to the dorsal telencephalon during embryonic development (Lepiemme et al., 2022). Whether this also stands for postnatal cortical OPC formation remains unknown. Role of BVs in astrocyte progenitor's migration is still to be determined. A significant part of cortical Alhd1l1-positive

cells, which include differentiated astrocytes as well as progenitors, are in contact with BVs at P1, but this population drops at P5, in the middle of the highly proliferative and migratory phase of astrocyte progenitors (Clavreul et al., 2019; Freitas-Andrade et al., 2023). BVs have also been shown as a signalling source for both oligodendrocyte and astrocyte maturation (Paredes et al., 2021).

In this study, we developed *VeCell*, a new Fiji plugin to characterize macroglial cell density, distribution and distance to BVs in the developing and mature brain. Macroglial cells were immunolabelled for the high-mobility-group transcriptional factors Sox 9 and 10 which regulate astrocyte and oligodendrocyte differentiation from glial precursors (Stolt and Wegner, 2010). Sox9 is expressed in NPCs and controls their switch to glial progenitors (Güven et al., 2020; Kang et al., 2012; Stolt, 2003). Its expression decreases during OligoLC specialisation, while increasing in astrocytes (Nagao et al., 2016; Klum et al., 2018). Sox10 is expressed in all OligoLCs, which are, during postnatal development, a mix of OPCs from embryonic ventral origins, OPCs originated from postnatal cortical progenitors and mature oligodendrocytes. In these cells, Sox10 regulates the transcription of myelin-forming genes (Foerster et al., 2024; Stolt et al., 2002).

Focusing on the somatosensory cortex, we found that Sox9+ cell density is homogeneous across cortical layers and strongly decreases after P5, while Sox10+ cell density is maintained across postnatal development and is always higher in the deeper layers of the cortex. Distribution analysis using the cumulative distribution function of nearest-neighbour distances revealed that Sox9+ cells are distributed regularly within the parenchyma from P5. Inversely, Sox10+ cells are more randomly distributed during postnatal development, with varying distance between cells. Our analysis of the cortical vascular network confirmed the increased volume between P5 and P15, together with an increased branching. Finally, we showed that both Sox9+ and Sox10+ cells are closer to BVs at later developmental stages.

Results

Cortical density of macroglial cells across postnatal development

To characterize the postnatal development of cortical macroglial cells *in situ,* we immunolabelled brain sections from postnatal day (P) 5, P15 and P60 for the transcription factors Sox9 and Sox10, focusing our study on the somatosensory cortex (Fig. 1A). Cell detection was automated using an adapted version of the CellPose deep learning-based algorithm and Fiji software (Schindelin et al., 2012; Stringer et al., 2021). After model training on a dataset of 28 images collected across three developmental stages, positive cells were detected with >85% accuracy (Fig. 1F and Methods). Given previous studies showing different population dynamics across cortical layers (Orduz et al., 2019), we analysed the upper (Bin 1) and lower (Bin 2) parts of the cortex separately, based on cell density revealed by nuclear labelling (Fig. 1B).

In the cortex, Sox9+ cells are predominantly composed of glial progenitors at P5 and are largely restricted to cells from astroglial lineage at P15 and P60 (Fig. 1A). No difference in Sox9+ cell density was observed between the upper and lower cortical parts at any developmental stage (Fig. 1C, D, G Table S1). However, the density dropped significantly between P5 and P60 (Kruskal-Wallis test, p=0.004). This effect was particularly pronounced between P5 and P15 with a 2.3-fold decrease in Sox9+ cell density in Bin 1 (P5: 1132±43; P15: 492±51; P60: 286±32 $10^2/mm^3$ cells) and a 2.4-fold decrease in Bin 2 (P5: 1102±80; P15: 451±69; P60: 422.8±27 $10^2/mm^3$ cells).

For Sox10+ OligoLC cells, significant differences in density were observed within the cortex. A higher density of Sox10+ cells was consistently found in the lower part of the cortex, near the corpus callosum, at all stages of postnatal development (Fig. 1C, E, H, Table S1). A small reduction in Sox10+ cell density was observed in the upper part (Bin 1, Kruskal-Wallis test, p-value=0.03) but not in the lower part of the cortex (Bin 2, Kruskal-Wallis test, p-value=0.2). Of note, these densities were consistent with previous studies (Orduz et al., 2019).

When comparing the two cell populations, Sox9+ cells were always more abundant than Sox10+ cells in the upper part of the cortex, in particular at P5 when three times more Sox9+ cells were detected. In the lower part, while Sox9+ cells were more abundant at P5, Sox10+ density was higher at P60 (Fig. 1C, H, Table S1).

Altogether, our *VeCell* Fiji plugin using the Cellpose algorithm enables the detection of macroglial cells based on Sox9 and Sox10 nuclear immunolabelling, revealing density disparities between these cell populations during postnatal development.

Distribution of macroglial cells in the cerebral cortex during postnatal development.

We next analysed the distribution of macroglial cells during postnatal development of the somato-sensory cortex. First, we measured the mean distance between each cell and its nearest neighbour. Consistent with the reduced density of Sox9+ cells after P5, the mean distance between neighbouring cells progressively increased during development (Bin 1; P5: 14.3±0.15; P15: 19.7±0.6; P60: 25.7±1.8 µm) (Bin 2; P5: 14.8±0.4; P15: 21.8±1.3; P60: 30.7±1.9 µm) (2-way ANOVA: p-value(age)<0.0001). Distances were similar in the upper and lower parts of the cortex, except at P60, where Sox9+ cells were closer to each other in the upper part (P60: Bin 1: 25.7±1.8; Bin 2: 30.7±1.9 µm, Sidak test, p-value=0.001) (Fig. 2A). To further characterize the distribution of Sox9+ cells, we measured the mean distance between each Sox9+ cell and its 10 nearest Sox9+ cells (Fig. 2B). Consistently, distance increased progressively during development (Bin 1: P5: 31.9±0.6; P15 43±1.9; P60 54.2±4 µm) (Bin 2: P5: 33.3±1.1; P15 47.1±3.3; P60 67.5±4.6 µm) (2-way ANOVA: p-value(age)<0.0001). Significant differences between cortical parts were only observed at P60 (Sidak test, p-value=0.0004).

For Sox10+ cells, no difference in the mean distance between adjacent cells were observed across postnatal development (2-way ANOVA: p-value=0.5) (Fig. 2C). Consistent with density differences, Sox10+ cells were closer to each other in the lower part of the cortex (2-way ANOVA; closest cell: p-value <0.0001, 10 closest-cells: p-value = 0.0004) (Fig. 2C, D and Table S1).

The spatial distribution of cells within a population can exhibit patterns ranging from clustering to regular spacing, which may reflect distinct developmental mechanisms such as repulsion or attraction. To address this, we used the *2D/3D Spatial Analysis* Fiji plugin to assess deviation from spatial randomness (Andrey et al., 2010) (Methods). Specifically, we computed the G-function, the cumulative distribution function (CDF) of the distance between a typical point (the labelled cell) and its nearest-neighbour. Shorter distances suggest clustering, while longer distances indicate regular spacing (Fig. 2E). The experimental CDF was compared to the CDF of randomly generated point patterns within the same area and with the same number of points. For each region of interest (ROI), this comparison was computed

as the Spatial Distribution Index (SDI) (Andrey et al., 2010). Distribution of SDIs in each experimental condition indicates the cell distribution pattern: uniformly distributed SDIs (0-1) reflects a random distribution of cells, values near 0 suggest clustering, and values near 1 indicate regular spacing (Andrey et al., 2010) (Fig. 2E).

Given the higher density of Sox10+ cells in the lower part of the cortex, we focused our study on this region (Fig. 1). For Sox9+ cells, the SDI distribution was significantly different from the random distribution at all stages (Kolmogorov-smirnov test, p-value<0.0001) (Fig. 2F; Table S1) and consistently close to 1 across development (Bin 2: P5: 1±0; P15: 0.99±0.03; P60: 0.99±0.03) with no difference across stages (Kruskal Wallis test, p-value =0.7). These results indicate that Sox9+ cells are regularly organized, maintaining consistent spacing at all postnatal developmental stages. For Sox10+ cells, the SDI distribution was significantly different from random at P5 (Kolmogorov-smirnov test, p-value = 0.005), but not at P15 or P60 (Kolmogorov-smirnov test, $p\text{-value}_{P15}>0.1$; $p\text{-value}_{P60}>0.1$), suggesting that the Sox10+ population adopt a more random organization during development.

Overall, our findings demonstrate that Sox9+ and Sox10+ cells follow distinct postnatal trajectories and adopt different organizational patterns in the somatosensory cortex. Sox9+ cells consistently maintain a regular distribution and stable density, while Sox10+ cells are more concentrated in deeper cortical layers and exhibit a more random spatial arrangement, with variable intercellular distances.

Distribution of glial cells relative to the vascular compartment

Macroglial cells are closely associated with the brain vasculature. In the adult CNS, astrocytes entirely cover the BVs through specialized processes called endfeet or perivascular astrocyte processes (PvAP) (Cohen-Salmon et al., 2020). During development, the formation of PvAPs, which occurs from birth to P15, plays a crucial role in BV maturation (Freitas-Andrade et al., 2023; Gilbert et al., 2021, 2019). Furthermore, some OPCs migrate along BVs during embryonic development (Lepiemme et al., 2022).

To better understand the relationship between macroglial cells and BVs during postnatal development we analysed the distance between these cells and BVs in the somatosensory cortex. In addition to Sox9 or Sox10, BVs were immunolabeled for Pecam-1/CD31. BV detection was implemented in the *VeCell* Fiji plugin, enabling analysis of (i) vascular volume, (ii) vascular network branching and (iii) the distance between macroglial cells and their nearest BV (Fig. 3).

The cortical vascular volume, normalized by the cortical volume to account for cortical expansion, was analysed at P5, P15 and P60 brain sections. A global increase in vascular volume was observed between P5 and P15 (Fig. 3D), consistent with postnatal angiogenesis and capillary bed extension (Coelho-Santos and Shih, 2020) (Bin 1; P5: 0.09±0.01; P15: 0.1±0.02 $\mu m^3/\mu m^3$; Tukey's test: p-value=0.0006) (Bin 2; P5: 0.08±0.01; P15: 0.1±0.01 $\mu m^3/\mu m^3$; Tukey's test p-value = 0.0002). After P15, vascular volume decreased, probably due to the unfinished cortical volume growth (Tukey's test, $p\text{-value}_{Bin\ 1}$=0.0006; $p\text{-value}_{Bin\ 2}$=0.0002). Branching of the vascular network also increased significantly between P5 and P15 (Fig. 3F) (Bin 1; P5: 396.3±36.82; P15: 701.1±140.5 branches/μm^3 of BVs; Tukey's test p-value <0.0001) (Bin 2: P5: 348.2±33.31; P15: 550.4±73.85 branches/μm^3 of BVs; Tukey's test p-value = 0.0001). Vascular volume (two-way ANOVA, p-value =0.001) and branching (two-way ANOVA, p-value =0.0004) were consistently reduced in the lower part of the cortex compared to the upper part (Fig. 3D, F).

Next, we calculated the distance between each macroglial cell and its nearest BV (Fig. 3A, G and H) (Table S1). Both Sox9+ and Sox10+ cells were closer to BV at P15 compared to P5. At P5, both Sox9+ and Sox10+ cells were closer to BVs in the upper cortical part compared to the lower. However, no such differences were observed at later developmental stages. Interestingly, while Sox9+ and Sox10+ cells were at a similar distance to BVs at P5 (Bin 1; d_{Sox9} = 11.1±0.5, d_{Sox10}=11.4±0.4 µm; T-Test p-value = 0.46) (Bin 2; d_{Sox9} = 15.5±1.5, d_{Sox10}=14.7±1.3 µm; T-Test p-value = 0.51), Sox9+ cells were closer to BVs than Sox10+ cells at P60 (Bin 1, d_{Sox9}= 6.4±0.6, d_{Sox10}=8.6±0.8 µm; T-Test p-value = 0.02) (Bin 2; d_{Sox9} = 8.2±0.7, d_{Sox10}=10.4±0.3 µm; T-Test p-value = 0.006).

We developed a robust tool to study the relationship between macroglial cells and BVs. Our analysis confirms an increased vascular density and branching between P5 and P15 in the somatosensory cortex, with higher vascular density and branching observed in the upper cortical layers. Additionally, we show that the distance between macroglial cells and BVs decreases after P5. Notably, in the mature cortex, Sox9+ cells are closer to BVs than Sox10+ cells, suggesting distinct interactions between these macroglial populations and the vasculature.

Discussion

Using a newly developed Fiji plugin, *VeCell*, we describe the distribution of macroglial cells during postnatal development, based on the labelling of two transcription factors, Sox9 and Sox10. At P5, Sox9 is expressed by glial progenitors and becomes progressively more restricted to astrocytes. Sox10 is specific to the oligodendrocyte lineage and is expressed by OPC as well as mature oligodendrocytes.

The density of Sox9+ cells was lower at P15 compared to P5, which may be linked to the reduction in macroglial cell density during this period of intense neuronal production (Bandeira et al., 2009). Additionally, this decrease could be attributed to the reduced expression of Sox9 as some glial progenitors differentiate into OligoLC (Klum et al., 2018). Consistently, our data show that the density of Sox9+ cells was higher than that of Sox10+ cells at P5, but this difference no longer held at P60. Interestingly, similar trends were observed when using Aldh1l1, an astrocyte-specific marker (Freitas-Andrade et al., 2023).

In parallel, the density of Sox10+ cells remained stable throughout postnatal development in the lower part of the somatosensory cortex. Given the increase in cortical thickness, this stability reflects an increase in the total number of cells. The production of postnatal OligoLC thus extends beyond the replacement of the embryonically derived OPC population (Kessaris et al., 2006). It also reflects the ongoing postnatal balance between the proliferation of OPCs and their differentiation into myelinating oligodendrocytes, particularly from P9 onwards (Fletcher et al., 2021). The Sox10+ population was less dense in the upper part of the somatosensory cortex, at all developmental stages, as previously described for OPC (Ogino et al., 2020). This specific organisation of OPC has been shown to depend on Reelin, which is secreted by Cajal-retzius cells during late embryonic development and acts as a driving force for OPC migration, along with other chemotactic signals (Barber et al., 2022; Ogino et al., 2020). This pattern is also consistent with the known higher density of myelinating oligodendrocytes in the lower cortical layers (Orduz et al., 2019).

In contrast, the density of Sox9+ cells remained similar across cortical layers at all stages studied. This is in line with the previous observation that astrocytes completely tile the cortical parenchyma in the mature brain, with each cell occupying a similar volume (Halassa et al., 2007). Our data further suggest a coordinated colonization of the entire cortical parenchyma by macroglial progenitors/astrocytes beginning at P5.

To analyse the distribution of cells, we employed the *2D/3D Spatial Analysis* Fiji plugin originally designed for studying protein localization within the nucleus (Andrey et al., 2010). We showed that this tool could be adapted to analyse cell population within defined cortical areas. Our interest was on the organisation of different cell populations. We thus used the G-function, which measures the relationships between elements, rather than the F-function, which assesses organization within the tissue. Using this approach, we identified distinct organizational patterns for Sox9+ and Sox10+ cell population during postnatal development. Our analysis revealed that the Sox9+ population exhibits a regular distribution, indicating that these cells are evenly spaced. This aligns with the known organization of astrocytes, which occupy exclusive, non-overlapping domains (Bushong et al., 2004, 2002; Halassa et al., 2007). In contrast, Sox10+ cells were more randomly distributed within their cortical layers. This is consistent with previous studies reporting the presence of OPC doublets (Orduz et al., 2019).

The interaction between macroglial cells and BVs has gathered increasing interest in both developmental and disease contexts (Lepiemme et al., 2022; Niu et al., 2019; Watkins et al., 2014). Here, we present a tool to analyse BVs organisation in conjunction with macroglial cells across developmental stages using simple brain sections and low-resolution microscopy. Our analysis revealed changes in cortical BVs density and branching, with a peak at P15. This is in line with the second phase of postnatal angiogenesis and capillary formation (Coelho-Santos et al., 2021). The observed increase in BVs density was less pronounced than previously reported under similar conditions (Freitas-Andrade et al., 2023), likely due to differences in parameters for BVs volume detection.

We extended our plugin's functionality to calculate the distance from each cell to the nearest BV. Both Sox9+ and Sox10+ cells were found closer to BVs at P15/P60 compared to P5. This is similar to previous observations of increased Aldh1l1+ astrocytes density close to BVs at P14 compared to P5 (Freitas-Andrade et al., 2023). This result might simply reflect the increased BVs density in the parenchyma. However, we cannot rule out the possibility of active migration mechanism after P5, possibly driven by signals from vascular cells. However, this is against the notion of active migration along blood vessels during the astrocyte progenitor colonisation phase, which ends around P7 (Clavreul et al., 2019).

Interestingly, Sox9+ astrocyte cell bodies were closer to BVs than oligoLC. This is consistent with the close interaction between astrocytes and BVs, including the complete coverage of BVs with PvAPs by P15 (Gilbert et al., 2021; Mathiisen et al., 2010).

Figure legends

Figure 1. Macroglial cells density during postnatal cortical development.

A. Schematic representation of the studied area in the mouse brain (left) and developmental timeline (right) of the macroglial cells expressing Sox9 (red) or Sox10 (magenta). **B, C.** Representative Axio Zoom microscopy images of Hoechst (Blue), Sox9+ (red) or Sox10+ (magenta) showing the Region Of Interest (ROI) within the somato-sensory cortex (Bin 1: upper layers, Bin 2: lower layers). **D, E**. Spinning disk W1 Z-stack projection images of Sox9+ (red) (D) or Sox10+ (magenta) (E) cells detected by immunofluorescence at P5 and P60 in Bin 1 or Bin 2 of somatosensory cortical sections. **F**. Representative Axio Zoom microscopy Z-stack projection image of Sox9+ cells detected by immunofluorescence (top, white) on a P15 somatosensory cortical slice and the mask created by the *VeCell* Fiji plugin (down, red). **G, H.** Analysis of the Sox9+ (G) and Sox10+ (H) cells densities shown as a number of cells x10^2 per mm^3. N= 3 mice, n=1 section per animal, results are shown as mean of the results on 4 ROI ± SD. Statistics: Mann Whitney test between ages (G) or between layers (H).

Figure 2. Macroglial cells distribution during postnatal cortical development

A, B. Analysis of mean distance to the closest (A) or 10 closest (B) Sox9+ cells, shown as the mean distance for each cell of the studied area in the somato-sensory cortex. **C, D.** Analysis of mean distance to the closest (A) or 10 closest (B) Sox10+ cells, shown as the mean distance for each cell of the studied area in the somato-sensory cortex. **E**. Schematic summary of the G-function analysis of cell distribution. Cells can follow three main behaviours: grouped (SDI=0), randomly distributed or regularly spaced (SDI=1). The G-function is the cumulative distribution function (CDF) of the distance between a typical point (the labelled cell) in the pattern and it nearest-neighbour. The experimental CDF (black curve) is obtained for each ROI analysed and is compared to the CDF of randomly generated point patterns in the same area and with the same number of points (red curve). For each ROI analysed, comparison between the experimental and random CDF are computed as the Spatial Distribution Index (SDI). Distribution of SDIs in each experimental condition indicates the distribution pattern followed by the cells. **F**. Result of G-function analysis for Bin 2 Sox9+ (pink) and Sox10+ (purple) cells across postnatal development. N= 3 mice, n=1 section per animal, results are shown as mean of the results on 4 ROI (A-

D) per section or the result of one ROI (F) ± SD. Statistics: A-D: 2-way ANOVA; $p_{(age)}$: result of ANOVA for age effect; $p_{(Bin)}$: result of ANOVA for cortical layer effect. F: Kolmogorov-Smirnov test.

Figure 3. Macroglial cells distribution in relation to blood vessels during postnatal cortical development

A. Representative Axio Zoom microscopy Z-stack projection image of a P15 somatosensory cortical section stained for blood vessels (white) detected by immunofluorescence on Pecam-1 with the superimposed masks created by the VeCell Fiji plugin. BVs mask is in blue and Sox9+ cells are color coded for their distance to nearest BV from magenta (close to BV) to yellow (far from BV). a.i to a.iv are detailed of boxed area from A. a.i, immunofluorescence of Pecam-1-labeled BVs (white) and Sox9+ cells (red); a.ii, BVs mask created by the VeCell Fiji plugin (blue) superimposed to the Pecam-1 staining (white); a.iii, BVs mask created by the VeCell Fiji plugin (blue) superimposed to the Pecam-1 staining (white) and mask of Sox9+ cells color-coded for their distance to nearest BV; a.iv, skeleton mask of the BV for branching analysis (green). **B,C**. Representative Axio Zoom microscopy Z-stack projection images of P5 (B) and P15 (C) somatosensory cortical sections stained for blood vessels detected by immunofluorescence for Pecam-1 (white) and Sox9+ cells (red). **D**. Analysis of the vascular volume reported as BVs volume normalized by cortical volume. **E**. Representative Axio Zoom microscopy Z-stack projection images of P15 somatosensory cortical sections Bin1 (left) or Bin2 (right), stained for blood vessels detected by immunofluorescence for Pecam-1 (white). **F**. Analysis of the vascular branching as the number of 10^3 branches per mm^3 of BVs. **G, H.** Analysis of the distance to nearest vessels of Sox9+ (G) and Sox10+ (H) cells. N= 3 mice, n=1 (G, H) or 2 (D, F) sections per animal. Results are shown as mean of the results on 4 ROI per section ± SD. Statistics: 2-way ANOVA; p(age): result of ANOVA for age effect; p(Bin): result of ANOVA for cortical layer effect.

Materials and Methods

Animal experiments and ethical approval

C57BL/6JRj, aged 5 to 60 days were purchased from Janvier labs (Le Genest-Saint-Isle, France) and kept in pathogen-free conditions. All experiments and techniques complied with (i) the European Directive 2010/63/EU on the protection of animals used for scientific purposes and (ii) the guidelines issued by the French National Animal Care and Use Committee (reference: 2013/118). Animal cohorts were made of males and females.

Brain sections preparation

Mice were sacrificed by cervical dislocation or decapitation depending on mouse age. Brains were carefully collected and fixed in PBS/PFA 4% overnight at 4°C. After dehydration in 30% sucrose, brains were cut into 80-µm-thick sections using a Leitz (1400) cryomicrotome and kept at -20°C in storage solution (PBS/glycerol 30%/ethylene glycol 30%).

Immunofluorescent staining

Brain sections were rinsed three times 15 min in PBS and incubated in a blocking solution (BS) for 1h at room temperature (RT). BS were PBS/normal goat serum 5%/Triton X-100 0.5% (Sox10) or PBS/Triton X-100 0.5% (Sox9). Sections were incubated with primary antibodies diluted in the same BS at 4°C overnight. After three rinses of 15 min in PBS, the sections were incubated for 2h at RT with secondary antibodies and Hoechst reagent, rinsed in PBS, and mounted in Fluoromount G (Southern Biotech, Birmingham, AL). Images were acquired using a wide-field Axio Zoom V16 microscope and its Apotome V2 module (Zeiss) or spinning disk W1 (Nikon).

Primary and secondary antibodies

Primary antibodies used were polyclonal goat IgG anti-Sox9 (AF3075 Biotechne/R&D, 1:500), monoclonal mouse/IgG2a anti-Sox10 (66786-1-Ig Proteintech, 1:500), AlexaF647-coupled Polyclonal Goat IgG anti-Pecam-1/Cd31 (AF3628R-MTO, Biotechno, 1:200). Secondary antibodies used were AlexaF555-coupled Goat anti-mouse IgG2a (A-21137 thermo Fisher, 1:1000) and AlexaF555-coupled Donkey anti-Goat IgG (A-21432 thermo Fisher, 1:1000). Nuclei were stained using Hoechst (Thermo fisher 62249, 1/2000).

Image analysis

Bins used to draw the ROI were defined based on cell density using nuclear staining Hoechst as presented in Figure 1A. Bin 1 corresponds to the upper part of the cortex, Bin 2 to the deeper part. Layer 1 of the cortex was excluded because of its different organization and morphology of astrocytes.

The analysis was conducted in each region of interest using a custom-developed plugin called *VeCell* (https://github.com/orion-cirb/VeCell) for the Fiji software (Schindelin et al., 2012). This plugin integrates the Bio-Formats (Linkert et al., 2010), CLIJ (Haase et al., 2020) and 3D ImageJ Suite (Ollion et al., 2013) libraries. **VeCell** consists in three analysis steps.

1) Macroglial cell detection in the Sox9/Sox10 channel: detection is performed using the 2D-stitched version of the Cellpose algorithm (Stringer et al., 2021). A custom model was trained through the human-in-the-loop workflow available in the Cellpose GUI. This model was initialized with the 'cyto2' pre-trained Cellpose model and fine-tuned using a dataset of 36 images collected across three developmental stages (P5, P15, and P60). Of these, 8 images were reserved for validation. The model was trained using the following hyperparameters: learning rate = 0.1, weight decay = 0.0001, and number of epochs = 500. Training and validation loss curves were monitored to ensure convergence. Model performance was evaluated on a separate test set comprising 6 images (2 per developmental stage). The fine-tuned model achieved a significant improvement in mean average precision (mAP) at an IoU threshold of 0.5, increasing from 0.675 (for the 'cyto2' pretrained model) to 0.834. This model was deemed suitable for processing the entire dataset. During inference, the following parameters were used: diameter = 20, flow threshold = 0.4, cell probability threshold = 0.0**,** and stitching threshold = 0.5. Detected 3D cells were filtered based on volume to reduce false positives. Only cells with a volume between 300 µm³ and 3000 µm³ were retained for downstream analysis.

2) Blood vessel detection in the Pecam-1 channel: Images were normalized using the Quantile-Based Normalization algorithm ("'Quantile Based Normalization' ImageJ PlugIn," n.d.) ensuring intensity consistency across the dataset. A 3D median filter ($radius_x = 4$, $radius_y = 4$, $radius_z = 1$) was applied to reduce noise while preserving vessel borders. Subsequently, a slice-by-slice 2D Difference of Gaussians filter ($\sigma_1 = 4$, $\sigma_2 = 8$) was applied to enhance vessel structures. A binary mask was generated using the Triangle automated thresholding method. The process was repeated with a second 2D Difference of Gaussians filter ($\sigma_1 = 7$, $\sigma_2 = 14$), producing a second binary mask. These two binary masks

were then merged using a maximum point operation to ensure comprehensive vessel detection. Postprocessing includes applying a 3D closing filter *($radius_x$ = 8, $radius_y$ = 8, $radius_z$ = 1)* to fill gaps in vessel structures, followed by a 3D median filter *($radius_x$ = 1, $radius_y$ = 1, $radius_z$ = 1)* to smooth vessel borders. The resulting binary mask was labelled in 3D to identify individual vessel structures, which are filtered by volume to retain only vessels exceeding 600 μm^3. Finally, the binary mask was skeletonized using CLIJ library, and branches shorter than 30 µm were excluded to ensure only meaningful segments were included in subsequent skeleton analysis.

3) Computation and saving of metrics for macroglial cells and blood vessels. For macroglial cells, were calculated: volume, distance to the nearest neighbor, mean and maximum distances to the 10 nearest neighbors, distance to the nearest vessel, and nearest vessel's diameter. Additionally, spatial statistical analysis was performed to identify clustering or dispersion patterns within the macroglial cell population. This was achieved using the 2D/3D Spatial Analysis Fiji plugin from the 3D ImageJ Suite library, which computes the distance function G. This function represents the cumulative distribution of distances between a typical point in the spatial pattern and its nearest neighbor (Andrey et al., 2010). The spatial distribution index (SDI) is derived from this analysis, serving as a metric to quantify the deviation of the observed spatial distribution from a completely random distribution. For BVs, skeleton analysis was conducted using the Analyze Skeleton Fiji plugin (Arganda-Carreras et al., 2010). The following metrics are obtained: total volume, total length, mean branch length, number of branches and junctions, mean diameter and diameter standard deviation.

Statistical analysis

Data shown on graphs are expressed as means and SD. Graphs and statistical analyses were performed using Graphpad Prism 8.0.2 software. For every data, we first verified that they followed a normal distribution using Shapirow-Wilk test. If not, we used Kruskal Wallis and Mann-Whitney tests. If it is, we used a 2-way ANOVA followed by Sidak's multiple comparisons test to analyse differences between Bins or Tukey's multiple comparisons test, to analyse differences between ages. For SDI distribution, comparison to normality was performed using Kolmogorov-Smirnov test. Alpha thresholds for hypothesis verification were set at 0.05. The different statistical tests used are specified in the Figure legends and in the supplementary table 1.

Acknowledgments

We gratefully acknowledge the Orion technological core (IMACHEM-IBiSA) of Center for Interdisciplinary Research in Biology for their support, and especially Estelle Anceaume and Julien Dumont for assisting us with the Axio Zoom microscopy image acquisition. We thank the whole "physiology and physiopathology of the gliovascular unit" team for helpful comments and contribution on the VeCell plugin functionality.

References

Andrey, P., Kiêu, K., Kress, C., Lehmann, G., Tirichine, L., Liu, Z., Biot, E., Adenot, P.-G., Hue-Beauvais, C., Houba-Hérin, N., Duranthon, V., Devinoy, E., Beaujean, N., Gaudin, V., Maurin, Y., Debey, P., 2010. Statistical Analysis of 3D Images Detects Regular Spatial Distributions of Centromeres and Chromocenters in Animal and Plant Nuclei. PLOS Computational Biology 6, e1000853. https://doi.org/10.1371/journal.pcbi.1000853

Arganda-Carreras, I., Fernández-González, R., Muñoz-Barrutia, A., Ortiz-De-Solorzano, C., 2010. 3D reconstruction of histological sections: Application to mammary gland tissue. Microscopy Research and Technique 73, 1019–1029. https://doi.org/10.1002/jemt.20829

Bandeira, F., Lent, R., Herculano-Houzel, S., 2009. Changing numbers of neuronal and non-neuronal cells underlie postnatal brain growth in the rat. Proceedings of the National Academy of Sciences 106, 14108–14113. https://doi.org/10.1073/pnas.0804650106

Barber, H.M., Ali, M.F., Kucenas, S., 2022. Glial Patchwork: Oligodendrocyte Progenitor Cells and Astrocytes Blanket the Central Nervous System. Front. Cell. Neurosci. 15. https://doi.org/10.3389/fncel.2021.803057

Bushong, E.A., Martone, M.E., Ellisman, M.H., 2004. Maturation of astrocyte morphology and the establishment of astrocyte domains during postnatal hippocampal development. International Journal of Developmental Neuroscience 22, 73–86. https://doi.org/10.1016/j.ijdevneu.2003.12.008

Bushong, E.A., Martone, M.E., Jones, Y.Z., Ellisman, M.H., 2002. Protoplasmic astrocytes in CA1 stratum radiatum occupy separate anatomical domains. The Journal of neuroscience 22, 183–192.

Clavreul, S., Abdeladim, L., Hernández-Garzón, E., Niculescu, D., Durand, J., Ieng, S.-H., Barry, R., Bonvento, G., Beaurepaire, E., Livet, J., Loulier, K., 2019. Cortical astrocytes develop in a plastic manner at both clonal and cellular levels. Nature Communications 10, 4884. https://doi.org/10.1038/s41467-019-12791-5

Coelho-Santos, V., Berthiaume, A.-A., Ornelas, S., Stuhlmann, H., Shih, A.Y., 2021. Imaging the construction of capillary networks in the neonatal mouse brain. Proceedings of the National Academy of Sciences 118, e2100866118. https://doi.org/10.1073/pnas.2100866118

Coelho-Santos, V., Shih, A.Y., 2020. Postnatal development of cerebrovascular structure and the neurogliovascular unit. WIREs Developmental Biology 9, e363. https://doi.org/10.1002/wdev.363

Cohen-Salmon, M., Slaoui, L., Mazaré, N., Gilbert, A., Oudart, M., Alvear-Perez, R., Elorza-Vidal, X., Chever, O., Boulay, A.-C., 2020. Astrocytes in the regulation of cerebrovascular functions. Glia. https://doi.org/10.1002/glia.23924

Engelhardt, B., 2003. Development of the blood-brain barrier. Cell Tissue Res 314, 119–129. https://doi.org/10.1007/s00441-003-0751-z

Fletcher, J.L., Makowiecki, K., Cullen, C.L., Young, K.M., 2021. Oligodendrogenesis and myelination regulate cortical development, plasticity and circuit function. Seminars in Cell & Developmental Biology, Special issue: Cortical Development edited by Helen Cooper and Cecilia Flores / Special issue: Heart generation and regeneration edited by Chulan Kwon and Emmanouil Tampakakis 118, 14–23. https://doi.org/10.1016/j.semcdb.2021.03.017

Foerster, S., Floriddia, E.M., van Bruggen, D., Kukanja, P., Hervé, B., Cheng, S., Kim, E., Phillips, B.U., Heath, C.J., Tripathi, R.B., Call, C., Bartels, T., Ridley, K., Neumann, B., López-Cruz, L., Crawford, A.H., Lynch, C.J.,

Serrano, M., Saksida, L., Rowitch, D.H., Möbius, W., Nave, K.-A., Rasband, M.N., Bergles, D.E., Kessaris, N., Richardson, W.D., Bussey, T.J., Zhao, C., Castelo-Branco, G., Franklin, R.J.M., 2024. Developmental origin of oligodendrocytes determines their function in the adult brain. Nat Neurosci 27, 1545–1554. https://doi.org/10.1038/s41593-024-01666-8

Freitas-Andrade, M., Comin, C.H., Van Dyken, P., Ouellette, J., Raman-Nair, J., Blakeley, N., Liu, Q.Y., Leclerc, S., Pan, Y., Liu, Z., Carrier, M., Thakur, K., Savard, A., Rurak, G.M., Tremblay, M.-È., Salmaso, N., da F. Costa, L., Coppola, G., Lacoste, B., 2023. Astroglial Hmgb1 regulates postnatal astrocyte morphogenesis and cerebrovascular maturation. Nat Commun 14, 4965. https://doi.org/10.1038/s41467-023-40682-3

Ge, W.-P., Miyawaki, A., Gage, F.H., Jan, Y.N., Jan, L.Y., 2012. Local generation of glia is a major astrocyte source in postnatal cortex. Nature 484, 376–380. https://doi.org/10.1038/nature10959

Gilbert, A., Elorza-Vidal, X., Rancillac, A., Chagnot, A., Yetim, M., Hingot, V., Deffieux, T., Boulay, A.-C., Alvear-Perez, R., Cisternino, S., Martin, S., Taib, S., Gelot, A., Mignon, V., Favier, M., Brunet, I., Declèves, X., Tanter, M., Estevez, R., Vivien, D., Saubaméa, B., Cohen-Salmon, M., 2021. Megalencephalic leukoencephalopathy with subcortical cysts is a developmental disorder of the gliovascular unit.

Gilbert, A., Vidal, X.E., Estevez, R., Cohen-Salmon, M., Boulay, A.-C., 2019. Postnatal development of the astrocyte perivascular MLC1/GlialCAM complex defines a temporal window for the gliovascular unit maturation. Brain Struct Funct 224, 1267–1278. https://doi.org/10.1007/s00429-019-01832-w

Güven, A., Kalebic, N., Long, K.R., Florio, M., Vaid, S., Brandl, H., Stenzel, D., Huttner, W.B., 2020. Extracellular matrix-inducing Sox9 promotes both basal progenitor proliferation and gliogenesis in developing neocortex [WWW Document]. eLife. https://doi.org/10.7554/eLife.49808

Haase, R., Royer, L.A., Steinbach, P., Schmidt, D., Dibrov, A., Schmidt, U., Weigert, M., Maghelli, N., Tomancak, P., Jug, F., Myers, E.W., 2020. CLIJ: GPU-accelerated image processing for everyone. Nat Methods 17, 5–6. https://doi.org/10.1038/s41592-019-0650-1

Halassa, M.M., Fellin, T., Takano, H., Dong, J.-H., Haydon, P.G., 2007. Synaptic Islands Defined by the Territory of a Single Astrocyte. J. Neurosci. 27, 6473–6477. https://doi.org/10.1523/JNEUROSCI.1419-07.2007

Kang, P., Lee, H.K., Glasgow, S.M., Finley, M., Donti, T., Gaber, Z.B., Graham, B.H., Foster, A.E., Novitch, B.G., Gronostajski, R.M., Deneen, B., 2012. Sox9 and NFIA Coordinate a Transcriptional Regulatory Cascade during the Initiation of Gliogenesis. Neuron 74, 79–94. https://doi.org/10.1016/j.neuron.2012.01.024

Kessaris, N., Fogarty, M., Iannarelli, P., Grist, M., Wegner, M., Richardson, W.D., 2006. Competing waves of oligodendrocytes in the forebrain and postnatal elimination of an embryonic lineage. Nat Neurosci 9, 173–179. https://doi.org/10.1038/nn1620

Klum, S., Zaouter, C., Alekseenko, Z., Björklund, Å.K., Hagey, D.W., Ericson, J., Muhr, J., Bergsland, M., 2018. Sequentially acting SOX proteins orchestrate astrocyte- and oligodendrocyte-specific gene expression. EMBO reports 19, e46635. https://doi.org/10.15252/embr.201846635

Lepiemme, F., Stoufflet, J., Javier-Torrent, M., Mazzucchelli, G., Silva, C.G., Nguyen, L., 2022. Oligodendrocyte precursors guide interneuron migration by unidirectional contact repulsion. Science 376, eabn6204. https://doi.org/10.1126/science.abn6204

Linkert, M., Rueden, C.T., Allan, C., Burel, J.-M., Moore, W., Patterson, A., Loranger, B., Moore, J., Neves, C., MacDonald, D., Tarkowska, A., Sticco, C., Hill, E., Rossner, M., Eliceiri, K.W., Swedlow, J.R., 2010. Metadata matters: access to image data in the real world. Journal of Cell Biology 189, 777–782. https://doi.org/10.1083/jcb.201004104

Mathiisen, T.M., Lehre, K.P., Danbolt, N.C., Ottersen, O.P., 2010. The perivascular astroglial sheath provides a complete covering of the brain microvessels: an electron microscopic 3D reconstruction. Glia 58, 1094–1103. https://doi.org/10.1002/glia.20990

Miller, F.D., Gauthier, A.S., 2007. Timing Is Everything: Making Neurons versus Glia in the Developing Cortex. Neuron 54, 357–369. https://doi.org/10.1016/j.neuron.2007.04.019

Nagao, M., Ogata, T., Sawada, Y., Gotoh, Y., 2016. Zbtb20 promotes astrocytogenesis during neocortical development. Nat Commun 7, 11102. https://doi.org/10.1038/ncomms11102

Niu, J., Tsai, H.-H., Hoi, K.K., Huang, N., Yu, G., Kim, K., Baranzini, S.E., Xiao, L., Chan, J.R., Fancy, S.P.J., 2019. Aberrant oligodendroglial-vascular interactions disrupt the Blood Brain Barrier triggering CNS inflammation. Nat Neurosci 22, 709–718. https://doi.org/10.1038/s41593-019-0369-4

Ogino, H., Nakajima, T., Hirota, Y., Toriuchi, K., Aoyama, M., Nakajima, K., Hattori, M., 2020. The Secreted Glycoprotein Reelin Suppresses the Proliferation and Regulates the Distribution of Oligodendrocyte Progenitor Cells in the Embryonic Neocortex. J. Neurosci. 40, 7625–7636. https://doi.org/10.1523/JNEUROSCI.0125-20.2020

Ollion, J., Cochennec, J., Loll, F., Escudé, C., Boudier, T., 2013. TANGO: a generic tool for high-throughput 3D image analysis for studying nuclear organization. Bioinformatics 29, 1840–1841. https://doi.org/10.1093/bioinformatics/btt276

Orduz, D., Benamer, N., Ortolani, D., Coppola, E., Vigier, L., Pierani, A., Angulo, M.C., 2019. Developmental cell death regulates lineage-related interneuron-oligodendroglia functional clusters and oligodendrocyte homeostasis. Nat Commun 10, 4249. https://doi.org/10.1038/s41467-019-11904-4

Paredes, I., Vieira, J.R., Shah, B., Ramunno, C.F., Dyckow, J., Adler, H., Richter, M., Schermann, G., Giannakouri, E., Schirmer, L., Augustin, H.G., Ruiz de Almodóvar, C., 2021. Oligodendrocyte precursor cell specification is regulated by bidirectional neural progenitor–endothelial cell crosstalk. Nat Neurosci 24, 478–488. https://doi.org/10.1038/s41593-020-00788-z

"Quantile Based Normalization" ImageJ PlugIn [WWW Document], n.d. URL https://www.longair.net/edinburgh/imagej/quantile-normalization/ (accessed 12.10.24).

Schindelin, J., Arganda-Carreras, I., Frise, E., Kaynig, V., Longair, M., Pietzsch, T., Preibisch, S., Rueden, C., Saalfeld, S., Schmid, B., Tinevez, J.-Y., White, D.J., Hartenstein, V., Eliceiri, K., Tomancak, P., Cardona, A., 2012. Fiji: an open-source platform for biological-image analysis. Nat Methods 9, 676–682. https://doi.org/10.1038/nmeth.2019

Stolt, C.C., 2003. The Sox9 transcription factor determines glial fate choice in the developing spinal cord. Genes & Development 17, 1677–1689. https://doi.org/10.1101/gad.259003

Stolt, C.C., Rehberg, S., Ader, M., Lommes, P., Riethmacher, D., Schachner, M., Bartsch, U., Wegner, M., 2002. Terminal differentiation of myelin-forming oligodendrocytes depends on the transcription factor Sox10. Genes Dev. 16, 165–170. https://doi.org/10.1101/gad.215802

Stolt, C.C., Wegner, M., 2010. SoxE function in vertebrate nervous system development. The International Journal of Biochemistry & Cell Biology, SOX Transcription Factors 42, 437–440. https://doi.org/10.1016/j.biocel.2009.07.014

Stringer, C., Wang, T., Michaelos, M., Pachitariu, M., 2021. Cellpose: a generalist algorithm for cellular segmentation. Nat Methods 18, 100–106. https://doi.org/10.1038/s41592-020-01018-x

Watkins, S., Robel, S., Kimbrough, I.F., Robert, S.M., Ellis-Davies, G., Sontheimer, H., 2014. Disruption of astrocyte–vascular coupling and the blood–brain barrier by invading glioma cells. Nat Commun 5, 4196. https://doi.org/10.1038/ncomms5196

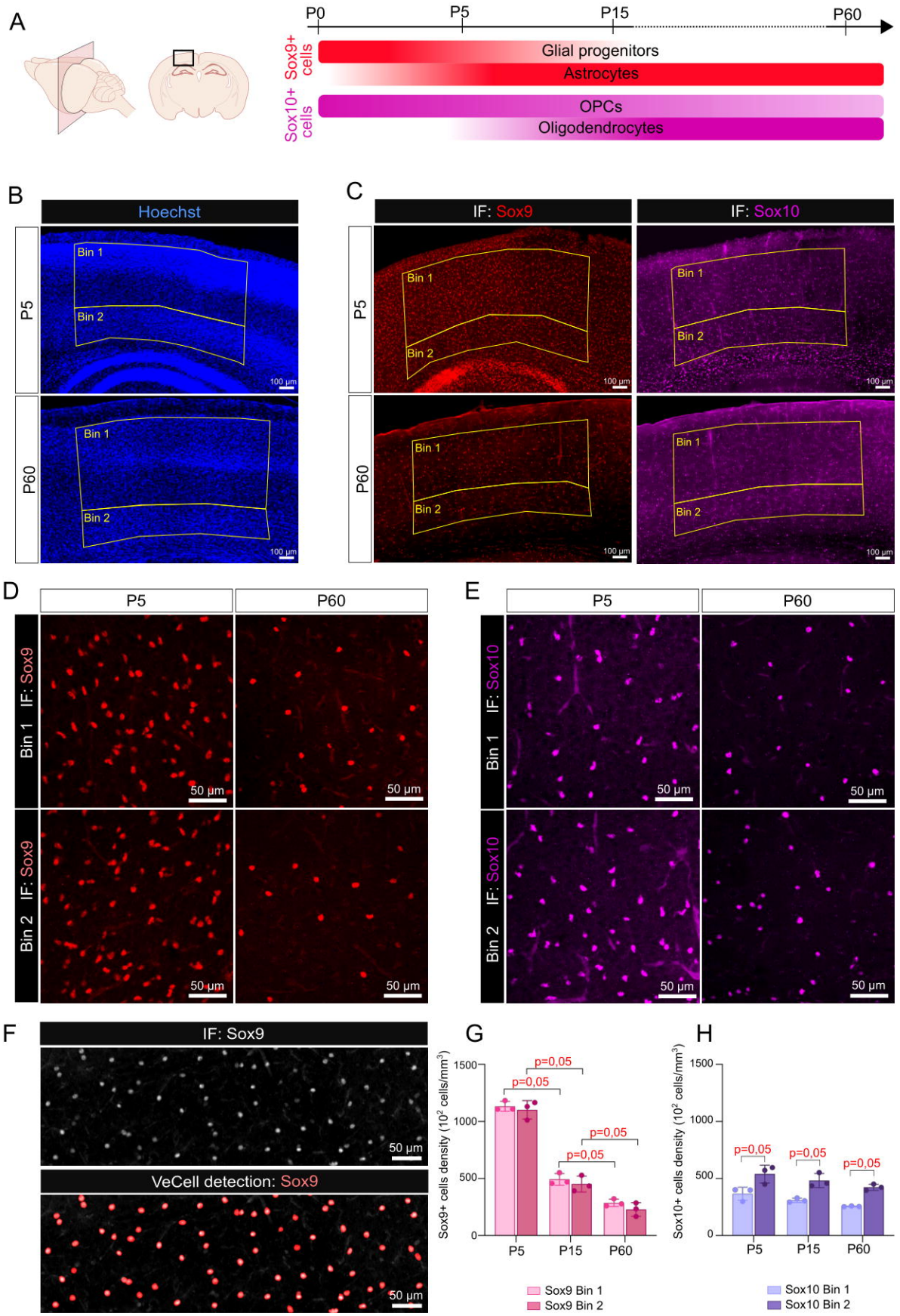
A
P0
P5
P15
P60
Sox9+ cells
Glial progenitors
Astrocytes
Sox10+ cells
OPCs
Oligodendrocytes
B
Hoechst
P5
P60
Bin 1
Bin 2
100 µm
C
IF: Sox9
IF: Sox10
D
P5
P60
IF: Sox9
Bin 1
Bin 2
50 µm
E
IF: Sox10
F
IF: Sox9
VeCell detection: Sox9
G
Sox9+ cells density (10² cells/mm³)
p=0,05
Sox9 Bin 1
Sox9 Bin 2
H
Sox10+ cells density (10² cells/mm³)
Sox10 Bin 1
Sox10 Bin 2

Figure 1

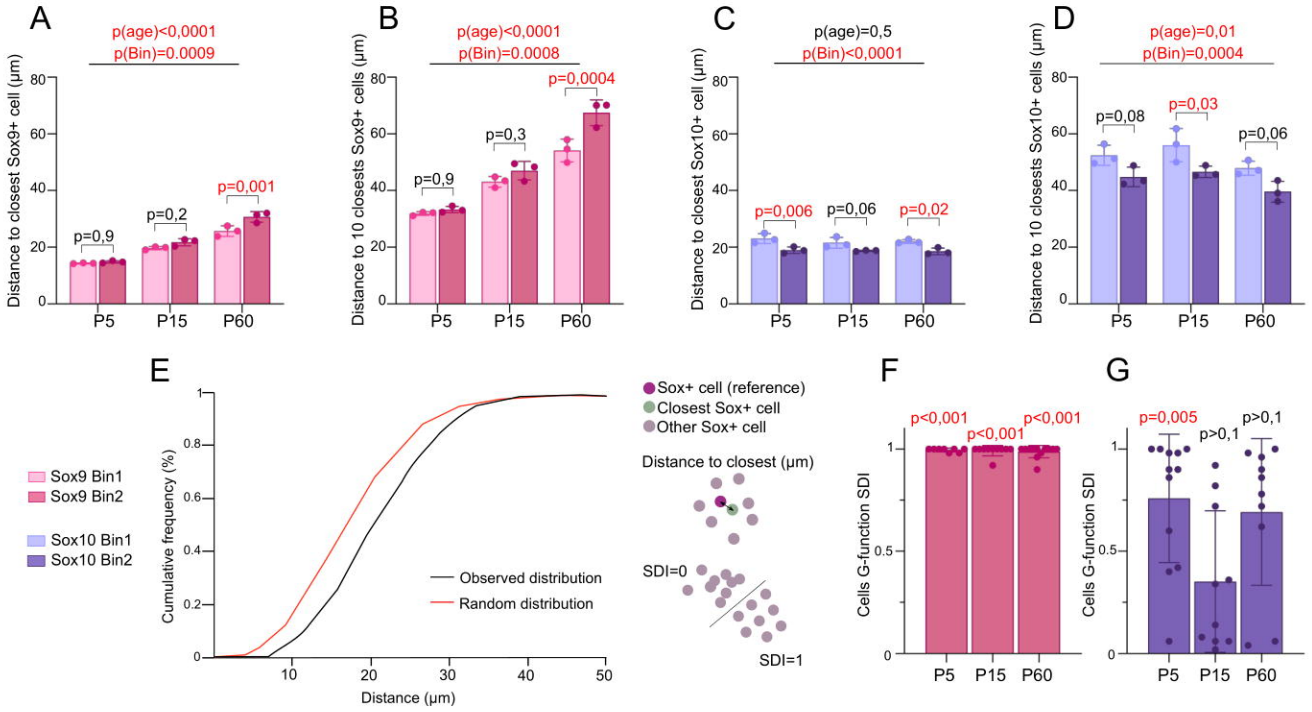
A
p(age)<0,0001
p(Bin)=0.0009
Distance to closest Sox9+ cell (µm)
p=0,9
p=0,2
p=0,001
P5
P15
P60
B
p(age)<0,0001
p(Bin)=0.0008
Distance to 10 closests Sox9+ cells (µm)
p=0,9
p=0,3
p=0,0004
C
p(age)=0,5
p(Bin)<0,0001
Distance to closest Sox10+ cell (µm)
p=0,006
p=0,06
p=0,02
D
p(age)=0,01
p(Bin)=0,0004
Distance to 10 closests Sox10+ cells (µm)
p=0,08
p=0,03
p=0,06
E
Sox9 Bin1
Sox9 Bin2
Sox10 Bin1
Sox10 Bin2
Cumulative frequency (%)
Observed distribution
Random distribution
Distance (µm)
Sox+ cell (reference)
Closest Sox+ cell
Other Sox+ cell
Distance to closest (µm)
SDI=0
SDI=1
F
p<0,001
p<0,001
p<0,001
Cells G-function SDI
G
p=0,005
p>0,1
p>0,1
Cells G-function SDI

Figure 2

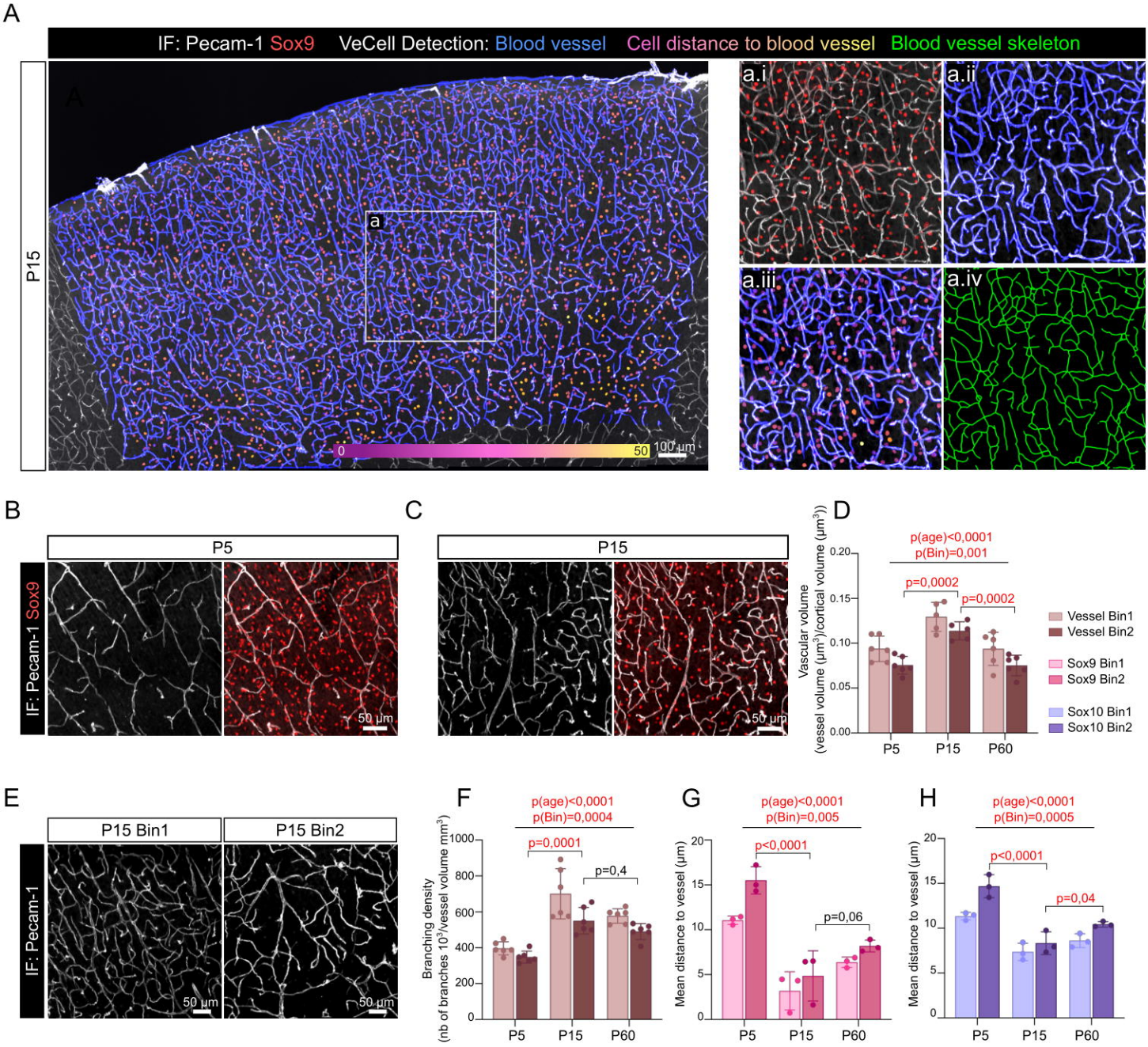
A
IF: Pecam-1 Sox9
VeCell Detection: Blood vessel
Cell distance to blood vessel
Blood vessel skeleton
P15
a
a.i
a.ii
a.iii
a.iv
0
50
100 µm
B
P5
IF: Pecam-1 Sox9
50 µm
C
P15
50 µm
D
p(age)<0,0001
p(Bin)=0,001
p=0,0002
p=0,0002
Vascular volume
(vessel volume (µm³)/cortical volume (µm³))
Vessel Bin1
Vessel Bin2
Sox9 Bin1
Sox9 Bin2
Sox10 Bin1
Sox10 Bin2
P5
P15
P60
E
P15 Bin1
P15 Bin2
IF: Pecam-1
50 µm
50 µm
F
p(age)<0,0001
p(Bin)=0,0004
p=0,0001
p=0,4
Branching density
(nb of branches 10⁻³/vessel volume mm³)
G
p(age)<0,0001
p(Bin)=0,005
p<0,0001
p=0,06
Mean distance to vessel (µm)
H
p(age)<0,0001
p(Bin)=0,0005
p<0,0001
p=0,04
Mean distance to vessel (µm)

Figure 3